Accepted Manuscript

Handling magnetic and structural properties of $EuMnO_3$ thin films by the combined effect of Lu doping and substrate strain

Y. Romaguera-Barcelay, F.G. Figueiras, J. Agostinho Moreira, J. Pérez-de-la-Cruz, P.B. Tavares, A. Almeida

PII: S0925-8388(18)31942-X

DOI: 10.1016/j.jallcom.2018.05.223

Reference: JALCOM 46199

To appear in: *Journal of Alloys and Compounds*

Received Date: 7 November 2017

Revised Date: 4 May 2018

Accepted Date: 20 May 2018

Please cite this article as: Y. Romaguera-Barcelay, F.G. Figueiras, J.A. Moreira, J. Pérez-de-la-Cruz, P.B. Tavares, A. Almeida, Handling magnetic and structural properties of $EuMnO_3$ thin films by the combined effect of Lu doping and substrate strain, *Journal of Alloys and Compounds* (2018), doi: 10.1016/j.jallcom.2018.05.223.

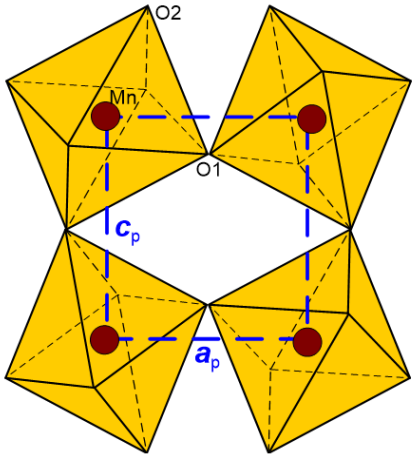

Bulk⇦$Eu_{1-x}Lu_xMnO_3$⇨**Film**

$0 \le x \le 0.2$	*Pmna*	$0 \le x \le 0.4$
4.14⇨4.13 Å	$a_p(x)$ >	4.11⇨4.07 Å
3.73⇨3.71 Å	$b_p(x)$ ≈	3.73⇨3.71 Å
3.78⇨3.76 Å	$c_p(x)$ ≈	3.78⇨3.74 Å
~146⇨142 °	Mn-O1-Mn <	~148⇨141 °
~2.0⇨~1.8 Å	Mn-O2 >	~1.9⇨~1.6 Å
AFM	Order <	AFM + FM

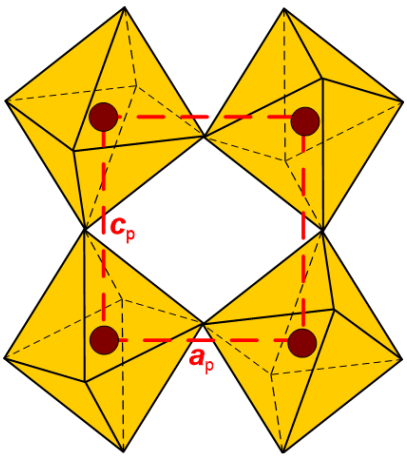

Handling Magnetic and Structural Properties of $EuMnO_3$ Thin Films by the Combined Effect of Lu Doping and Substrate Strain

Y. Romaguera-Barcelay [1,2], F. G. Figueiras [1,3,*], J. Agostinho Moreira [1], J. Pérez-de-la-Cruz [1], P. B. Tavares [4], A. Almeida [1]

** Corresponding author e-mail: ffigueiras@ua.pt*

[1] *IFIMUP and IN- Institute of Nanoscience and Nanotechnology, Physics Department, Sciences Faculty, University of Porto. Rua do Campo Alegre, 687, 4169-007 Porto. Portugal.*

[2] *Physics Department, Federal University of Amazonas, Manaus, Brazil*

[3] *Physics Department and CICECO-AIM, Aveiro University, 3810-193 Aveiro, Portugal*

[4] *CQVR and Chemistry Department, University of Trás-os-Montes & Alto Douro, 5001-801 Vila Real, Portugal.*

ABSTRACT

This work aims to understand the alterations induced by film/substrate lattice mismatch in structure, lattice dynamics and magnetic response of orthorhombic $Eu_{1-x}Lu_xMnO_3$ thin films within the range $0 \leq \mathbf{x} \leq 0.4$, when compared to results reported for ceramics with analogous composition. Thin films, which have been deposited onto Pt/Ti/SiO2/Si(100) oriented substrates via chemical method, exhibit noteworthy modifications in the magnetic ordering properties and, contrary to ceramics, do not show any sharp phase transition to the paramagnetic state. This reveals an induced ferromagnetic response in the films which is stable up to 100 K. X-ray diffraction and Raman spectroscopy measurements have been performed to identify the mechanically compressive state induced by the substrate and Lu doping. This facilitates insight into the magnetoelastic coupling effect in these films which is driven by alterations in electronic orbital overlapping and the associated antiferromagnetic superexchange interactions.

INTRODUCTION

Transition metal oxides having strong correlated electrons systems (SCES) exhibit complex couplings between different degrees of freedom like lattice, charge, spins, phonons and orbitals. These materials continue to be an interesting field of research due to their vast range of physical properties. Of particular interest to explore are materials having multiferroic properties and magnetoelectric effects, both become appealing topics for fundamental physics and as proof of concept for potential technological applications [1-4]. Typical SCES materials like manganites, of the generic formula $LnMnO_3$, usually exhibit orthorhombic symmetry for larger Ln ionic radii, such as La, Pr, Nd, Sm, Eu, Gd, Tb and Dy [5], or hexagonal symmetry for smaller ionic radii, such as Ho, Er, Tm, Yb, Lu, besides Sc and Y [6]. Some of these rare-earth manganites present magnetic ordering with competing ferromagnetic (FM) and antiferromagnetic (AFM) exchanges, leading to modulated spin and lattice structures compatible with ferroelectricity [7, 8]. In detail, the orthorhombic $Eu_{1-x}Lu_xMnO_3$ system with $0 \leq \mathbf{x} \leq 0.3$ exhibit a rich phase diagram where a paramagnetic-paraelectric state above $\mathbf{T}_N = 52$ K for $\mathbf{x} = 0$ down to 45 K for $\mathbf{x} = 0.3$, below which an ordered AFM phase (AFM-1) appears with incommensurate collinear modulation of the manganese spins. For $\mathbf{x} < 0.1$ and $\mathbf{T} < 27$ K a weakly FM phase occurs with a canted A-type AFM order, although, this phase is not ferroelectric due to its collinear modulated structure. For $0.1 \leq \mathbf{x} \leq 0.2$, an antiferromagnetic phase (AFM-2) appears, which is also ferroelectric [9, 10]. The complexity of the $Eu_{1-x}Lu_xMnO_3$ phase diagram becomes the main motivation for exploring this system in the thin film form, examining how structural and magnetic properties can differ from those of ceramics due to strain effects induced by substrate. In addition, localized lattice mismatch observed at the interface between the Pt buffer and the Lu doped $EuMnO_3$ phase [11] is also expected to affect the response of these new series of films. The structural, dynamic, and magnetic properties will be ascertained by X-ray diffraction, Raman spectroscopy and magnetization measuring techniques. The results obtained for thin films deposited by sol-gel method onto oriented $Pt/Ti/SiO_2/Si(100)$ substrates will be compared with similar ones reported for ceramics in the same range of compositions. Moreover, comprehensive understanding of thin films phases, in relation compared to bulk form, is crucial for correct integration of materials into potential microelectronic applications.

MATERIALS and METHODS

$Eu_{1-x}Lu_xMnO_3$ thin films were prepared by sol-gel method, following the procedures detailed in references [11, 12]. Precursor solutions were prepared from europium (III) acetate hydrated (99.99%) and lutetium (III) nitrate hydrate (99.99%) dissolved in a 2:1 acetic/nitric acids molar mixture and afterward adding a stoichiometric molar content of manganese (II) acetate tetrahydrate (99.99%). The resulting solution was stabilized with pure 2-methoxyethanol until a final concentration of 0.2 molar. $Eu_{1-x}Lu_xMnO_3$ precursor solution was deposited onto $Pt/Ti/SiO_2/Si(100)$ substrates supplied by *Silicon Valley Microelectronics, Inc.* The selection of a typical Pt bottom electrode aims primarily to ensure good stability in high temperature oxidizing environments [13]. Each individual layer was deposited using a *Laurell WS-400-6NPP* automatic spin-coater at 3000 rpm during 60 seconds, dried for one minute at 80oC and pre-sintering at 400ºC during 10 minutes in a tubular furnace. Finally, the resulting pre-sintered films were annealed at 800ºC for an hour, followed by a quenching at 25ºC in air. Thin film samples surface and cross-section were analyzed by high resolution Scanning Electron Microscopy (FEG-ESEM) and X-Ray Energy-dispersive X-ray spectroscopy (EDS) using a *FEI Quanta 400 FEG ESEM / EDAX Genesis X4M*. Structural characterization of the films was carried out using a *PANalytical MRD* diffractometer equipped with Cu Kα radiation ($\boldsymbol{\lambda}$=1.5418 Å) source in Bragg-Brentano mode, with a 0.017º/10s step and 2$\boldsymbol{\theta}$ range from 20º to 80º. Rietveld refinements were performed using *FullProf* software in the profile matching mode [14]. Non-polarized micro-Raman spectra were recorded at room temperature in the 200-800 cm^{-1} spectral range. Linearly polarized 514.5 nm line of an Argon laser was used to excite the Raman signal with incident power on the sample kept below 10 mW in order to avoid local sample heating. The scattered light was analyzed by a *T64000 Jobin-Yvon* triple spectrometer operating in triple subtractive mode and equipped with a liquid-nitrogen-cooled charge coupled device. Identical conditions were maintained for all scattering measurements for both films and ceramic samples [9]. The spectral slit width was ~1.5 cm^{-1}. The observed Raman modes parameters (frequency, line width, amplitude) were obtained from the best fit of a sum of damped oscillator functions according to the formula [15].

$$I(w,T) = (1 + n(w,T)) \sum_{i=1}^{N} A_{0j} \frac{w\Omega_{0j}^2\Gamma_{0j}^2}{(\Omega_{0j}^2 - w^2)^2 + w^2\Gamma_{0j}^2} \qquad (1)$$

where $I(w,T)$ is the intensity of the disperse beam, $n(w,T)$ the Bose-Einstein factor, A_{0j} the oscillator strength, Ω_{0j} the wave number and Γ_{0j} the damping factor of the j^{th} oscillator. Magnetic properties were measured using a commercial superconducting quantum interference SQUID magnetometer in reciprocating sample option (RSO) mode with a sensitivity of ~10^{-7} emu. Samples were first cooled down to 5 K under 0 Oe zero field (ZFC run) and then under 100 Oe applied magnetic field cooling run (FC run), respective measurements were carried out in heating run from 5 to 300 K using a driving magnetic field of 100 Oe.

RESULTS and DISCUSSION

Micron scale SEM images of the surface of the $Eu_{1-x}Lu_xMnO_3$ ($0.0 \leq \mathbf{x} \leq 0.4$) thin film samples are shown on top row of Figure 1 a) to e), where is possible to observe a progressive growth of the typical grain size with increasing Lu doping, from below 0.5 µm for $\mathbf{x}$ = 0.0 up to over 1 µm for $\mathbf{x}$ = 0.4. This feature will be discussed further below. Bottom row of Figure 1 a) to e) show the correspondent films cross-section. Overall, cross-section images reveal a highly homogeneous and smooth film phase, without noticeable twining or cracks, with relatively uniform thickness below 200 nm. Moreover, the films even masks minor imperfections in the Pt buffer (lighter region) which attests the correct wetting and adhesion of the precursors during the deposition process. EDS results obtained for all samples are presented in table 1. Each film presents uniform appearance and chemical homogeneity throughout surface and no contributions from other contaminant elements was perceived, as exemplified in the EDS spectra of sample $\mathbf{x}$ = 0.4 shown in figure 2. Moreover, composition obtained by EDS for the films phase appears slight biased when compared to similar measurements performed in bulk ceramics, due to effects in electrons diffraction of the stratification and interfaces (absorption, secondary florescence), since the electron beam suffers additional interference when penetrating through thin film, buffers and substrate [16]. Hence, samples sorting relative to Lu percentage found by EDS ($\mathbf{x}_{EDS}$) follows the same trend as the intended for the nominal composition ($\mathbf{x}_{Nom}$) considering a systematic deviation or calibration by $\mathbf{x}_{Nom}$ ~$(1.29\mathbf{x}_{EDS} - 0.23)$ ±5% as depicted in figure 2 inset.

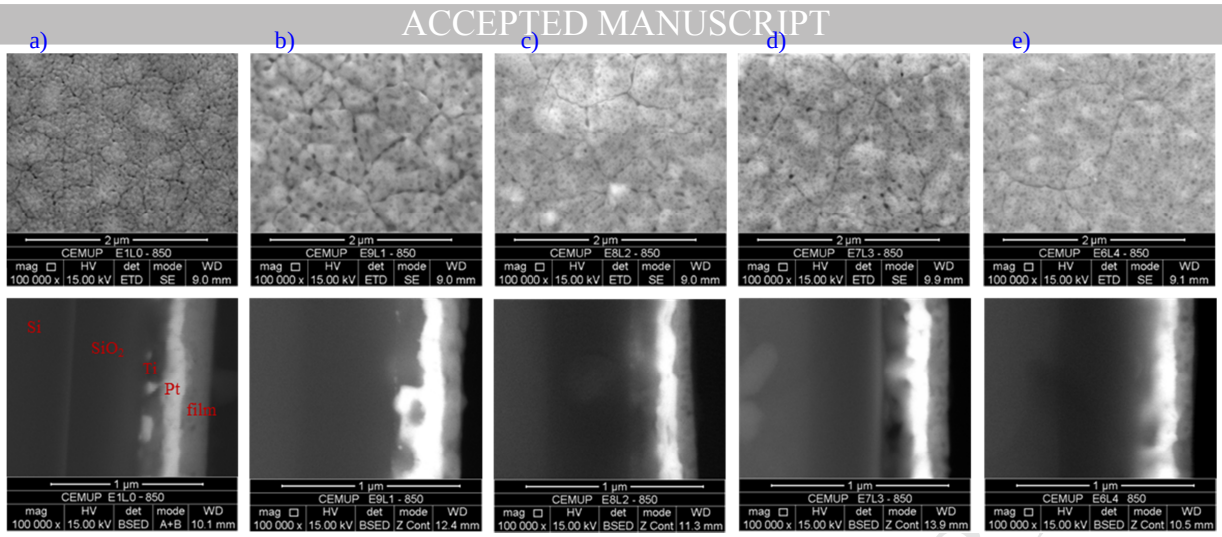

Figure 1: SEM images obtained for the series of $Eu_{1-x}Lu_xMnO_3$ thin films samples from a) to e) **x** = 0.0; 0.1; 0.2; 0.3; 0.4 respectively; top row) surface view and bottom row) cross-section.

x	EDS Peaks Net intensity (a.u.)							(At.)
	C *K*	**O** *K*	**Ti** *K*	**Eu** *L*	**Mn** *K*	**Lu** *L*	**Pt** *L*	**Lu/Eu** $\mathbf{x}_{EDS}$
0.1	14.20	85.83	15.94	**19.77**	30.30	**3.28**	25.28	**0.34**
0.2	18.02	103.5	19.82	**24.73**	32.50	**6.26**	23.50	**0.52**
0.3	11.48	113.2	17.36	**22.32**	42.76	**7.18**	21.42	**0.66**
0.4	15.16	111.2	18.54	**18.90**	42.36	**8.90**	23.22	**0.97**

Table 1: Net intensity of elements lines obtained from EDS spectra of each thin film samples and respective non-calibrated atomic proportion of Lu and Eu ($\mathbf{x}_{EDS}$).

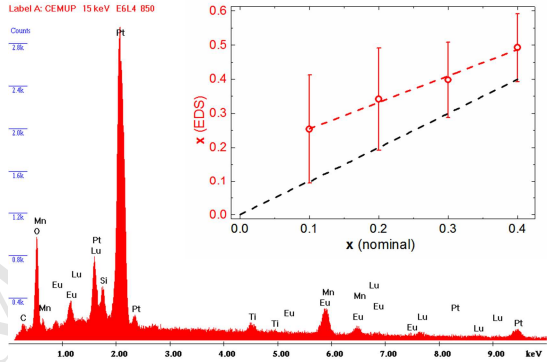

Figure 2: Example of EDS spectra obtain for **x** = 0.4 thin film. Inset: Plot of EDS results vs. nominal composition **x**.

Figure 3a) and 3b), where the peaks labelled with "*" are originated from the substrate, show representative examples of X-ray diffraction (XRD) patterns obtained at room temperature for the thin films with **x** = 0.1 and **x** = 0.4, along with the respective calculated patterns obtained from the Rietveld refinement. Figure 3c) enables a comparison to the XRD pattern of bulk $EuMnO_3$ with **Z** = 4 orthorhombic *Pnma* space group symmetry [10, 17]. The corresponding indexation evidences that the as-processed films have the same symmetry of the $EuMnO_3$ ceramic. The relatively higher intensity of reflection arising from the planes (002) at $2\boldsymbol{\theta}$ ~33.7º corresponds to the film phase preferential orientation in the direction [001] perpendicular to the substrate surface. The reflections from the film phase suffer a shift towards larger $2\boldsymbol{\theta}$ values as **x** increases, owing to unit cell volume reduction, this lattice contraction is expected from the substitution of Europium by Lutetium, due to the smaller ionic radius of Lu^{3+} (100.1 pm) compared to Eu^{3+} (108.7 pm) [18]. The calculated pseudo-cubic lattice parameters defined as $\boldsymbol{a}_p = \boldsymbol{a}_o/\sqrt{2}$, $\boldsymbol{b}_p = \boldsymbol{b}_o/2$ and $\boldsymbol{c}_p = \boldsymbol{c}_o/\sqrt{2}$ in the *Pnma* setting [19] are summarized in table 2. All compounds lattice parameters fulfil the relation $\boldsymbol{a}_p > \boldsymbol{c}_p > \boldsymbol{b}_p$ which is typically found in rare-earth manganites presenting the so-called ***O'*** structure associated with orbital ordering and Jahn-Teller cooperative distortions of the octahedral environment of the Mn^{3+} ions [19, 20].

Figures 4a) show the **x**-dependence of $\boldsymbol{a}_o$, $\boldsymbol{b}_o$, $\boldsymbol{c}_o$ for films and ceramics [10] respectively. It is possible to observe that the pseudo-cubic lattice parameters decrease as a linear function Lu concentration increases, in good agreement with the reduction of the effective A-site size. Moreover, whereas both $\boldsymbol{b}_p$ and $\boldsymbol{c}_p$ keep similar, $\boldsymbol{a}_p$ exhibits a significant reduction (~1%) in relation to those ones obtained for ceramics. This behavior is also reflected in **x**-dependence of the volume shown in figure 4b). Since the preferential growth orientation of the films is in the [001] direction, the decrease of $\boldsymbol{a}_p$ is favored by an in-plane compression along the [100] direction due to film-substrate lattice mismatch. The corresponding compression coefficients can be estimated from the slope of the lines fitted to the experimental data as depicted in figure 4 and summarized in table 3 for ceramics and films. In ceramics the relations $|\Delta\boldsymbol{a}_p/\Delta\mathbf{x}| < |\Delta\boldsymbol{b}_p/\Delta\mathbf{x}| < |\Delta\boldsymbol{c}_p/\Delta\mathbf{x}|$ are observed, whereas for films are ordered as $|\Delta\boldsymbol{b}_p/\Delta\mathbf{x}| < |\Delta\boldsymbol{a}_p/\Delta\mathbf{x}| < |\Delta\boldsymbol{c}_p/\Delta\mathbf{x}|$. The swop of order between the $\boldsymbol{a}_p$ and $\boldsymbol{b}_p$ axis

coefficients, corresponds to the in-plane compression of $\boldsymbol{a}_p$, resulting in a relative increase of $|\Delta \boldsymbol{a}_p/\Delta \mathbf{x}|$, whereas $|\Delta \boldsymbol{b}_p/\Delta \mathbf{x}|$ decreases, as the $\boldsymbol{b}_p$ axis undergoes a negligible stress induced by the slight larger cubic parameter of the Pt buffer ($\boldsymbol{a}_c^{Pt}$ = 3.9214 Å) [21]. In order to better describe these results, we have calculated the strain ($\boldsymbol{\varepsilon}$) in the films, taking the corresponding ceramic samples as comparison, through the expression:

$$\varepsilon(x) = \frac{a_p^{Film}(x) - a_p^{Bulk}(x)}{a_p^{Bulk}(x)} \qquad (2)$$

where $\boldsymbol{a}_p^{Film}(\mathbf{x})$ and $\boldsymbol{a}_p^{Bulk}(\mathbf{x})$ are respectively the pseudo-cubic parameters for a discrete **x**-value of the film and the ceramic. The **x**-dependence of $\boldsymbol{\varepsilon}$ also follows a linear expression as shown in the inset of Figure 4a, slightly decreasing with Lutetium concentration. Since the tension of the lattice mismatch between the film phase and the substrate is release by multiplying defects and grain boundaries, as Lu doping increases, it also tends to approach the pseudo-cubic lattice parameters of the film phase to those of the Pt buffer. Consequently, enabling grain size enlargement, as can be observed in the sequence of SEM images presented in figure 1 bottom row. It is worth noting that the reduction of the unit cell volume provides indication for substantial structural distortions, namely on the of oxygen octahedra tilting angles [22] beyond those found in ceramics.

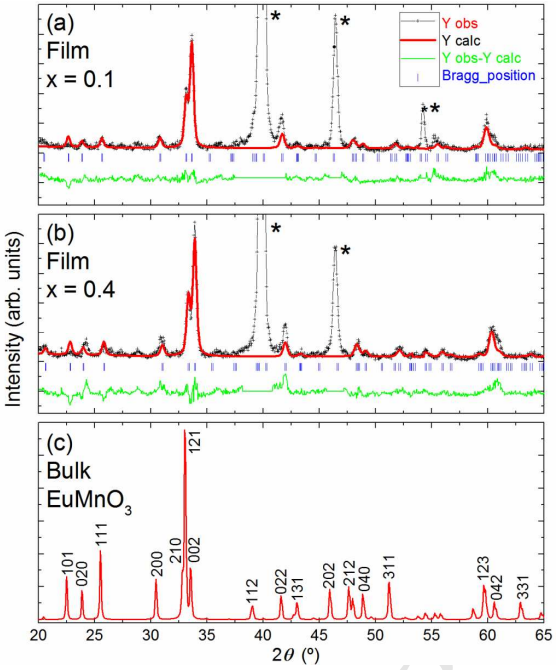

Figure 3: X-ray diffractograms of $Eu_{1-x}Lu_xMnO_3$ thin films for a) **x**=0.1, b) **x**=0.4 and. c) bulk $EuMnO_3$ [16]; "*" label reflections from substrate.

x	a_o (Å)	b_o (Å)	c_o (Å)	R_p	R_{wp}	χ^2
0.0	5.810	7.461	5.350	15.8	17.2	1.813
0.1	5.799(5)	7.451(9)	5.326(4)	7.8	10.2	2.655
0.2	5.781(5)	7.439(4)	5.308(1)	18.1	15.5	2.332
0.3	5.779	7.432	5.302	17.1	17.4	2.824
0.4	5.762	7.417	5.285	10.0	12.4	3.181

Table 2. Thin film phase *Pnma* crystallographic parameters obtained by Rietveld refinement of XRD diffractograms.

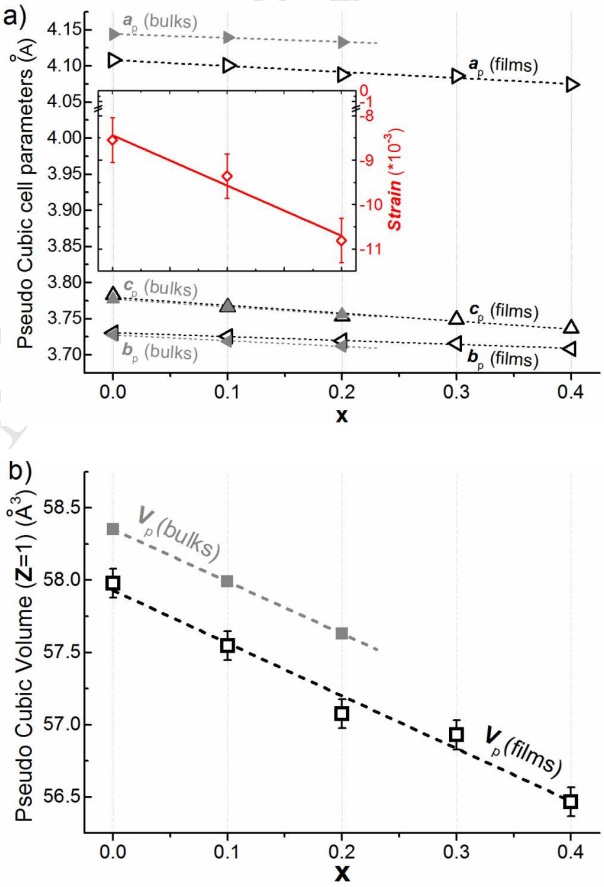

Figure 4: **x**-dependence for $Eu_{1-x}Lu_xMnO_3$ films (open symbols), and ceramics (solid symbols) [10] of the pseudo-cubic a) lattice parameters and b) volume. Inset) film strain along $\boldsymbol{a}_p$ (solid lines were obtained from the best fit of the linear function to the experimental data).

Figure 5 shows the non-polarized Raman spectra recorded at room conditions from 200 to 800 cm^{-1} of $Eu_{1-x}Lu_xMnO_3$ thin films for **x** = 0.0, 0.1, 0.2, 0.3, and 0.4. Excluding the modes observed at ~218 cm^{-1} and at ~690 cm^{-1}, which are addressed below, the spectra exhibit the main features characteristics of a *Pnma* structure, corroborating the results obtained by XRD. Raman-active modes of different polarizations emerge simultaneously due to the polycrystalline nature of the films, their assignment can be found in Ref. [23] and a specific analysis is provided in Ref. [13]. Two of the Raman modes are of particular importance since they can be used to monitor the main structural distortions occurring in thin films. The $A_g(4)$ band located between 350-400 cm^{-1}, which is assigned to the out-of-phase MnO_6 rotation mode around *Pnma* [101] direction; and the $B_{2g}(1)$ band observed between 600-630 cm^{-1} that is associated with the in-plane Mn-O2 symmetric stretching mode, activated by the *Jahn-Teller* distortion.

Pseudo-cubic parameter	Linear Fit **Films**	Linear Fit **Bulks**
$\boldsymbol{a}_p(\mathbf{x})$ =	(**4.108**±0.002) - (**0.082**±0.009).**x**	(**4.144**±0.001) - (**0.054**±0.008).**x**
$\boldsymbol{b}_p(\mathbf{x})$ =	(3.731±0.001) - (0.054±0.006).**x**	(3.728±0.001) - (0.078±0.003).**x**
$\boldsymbol{c}_p(\mathbf{x})$ =	(3.779±0.003) - (0.11 ±0.01).**x**	(3.778±0.001) - (0.105±0.001).**x**
$\mathbf{V}_p(\mathbf{x})$ =	(57.93±0.07) - (3.6 ± 0.3).**x**	(58.351±0.001) - (3.61 ± 0.01).**x**
$\boldsymbol{\varepsilon}(\mathbf{x})$ =	-(0.0084+0.0002) - (0.011 +0.001).**x**	

Table 3. Calculated linear fits of the pseudo-cubic perovskite crystallographic axis ($\boldsymbol{a}_p$, $\boldsymbol{b}_p$, $\boldsymbol{c}_p$) and of film strain ($\boldsymbol{\varepsilon}$) as function of **x**, obtained for the films and ceramics [10].

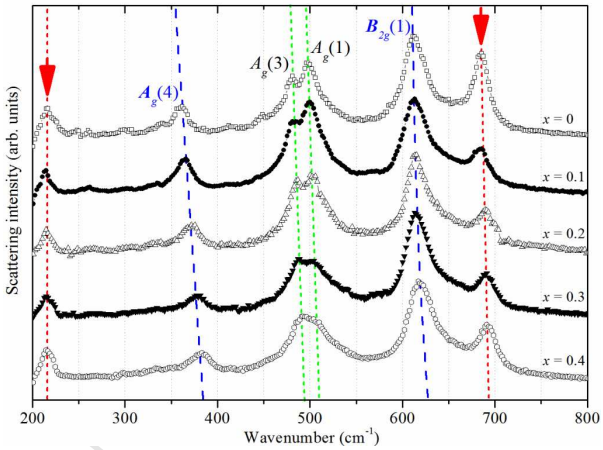

Figure 5: Non-polarized Raman spectra of $Eu_{1-x}Lu_xMnO_3$ for $0.0 \leq \mathbf{x} \leq 0.4$ and $EuMnO_3$ thin films recorded at room temperature. Mode assignment: $B_{2g}(1)$ in-plane Mn-O2 stretching mode; $A_g(1)$ Mn-O2 anti-stretching mode; $A_g(3)$ *Jahn-Teller* type symmetric stretching mode; $A_g(4)$ tilt mode of the MnO_6 octahedra. Arrows signalize two additional distortion infrared modes which are Raman activated.

The **x**-dependence of the $A_g(4)$ mode wavenumber for both films and ceramics [9] is shown in Figure 6a). This mode follows a linear increase with **x** for the two kinds of samples, though with a ~17% larger slope for the films. also shown in figure 6a) is the linear decrease of the apical Mn-O1-Mn bond angle with increasing **x**. It is know from previous works [9, 10] that the wavenumber of $A_g(4)$ mode is expected to scale with the apical Mn-O1-Mn bond angle. From this graph it is reckoned that the bond angle is in close correlation to the $A_g(4)$ mode wavenumber due to the relative reduction of the A-site atomic radius in the perovskite structure as Europium is gradually substituted by Lutetium [23, 24]. These relations are an indication that the magnitude of the Mn-O1-Mn bond angle is mainly determined by Lu concentration, whereas the larger values of the Mn-O1-Mn bond angle in films compared with those of ceramics are a direct consequence of the in-plane compression along the ***a***-direction with **x** due to the substrate effect. Moreover, the structure compression along the ***a***-axis is not compensated by in-plane elongation of the ***b***-axis neither in the orthogonal ***c***-axis, resulting a net increase of strain with **x** as seen in figure 4a) inset. Then, the question becomes, where the extra compressive elastic energy in the films is accommodated? In order to address this question, we have studied the **x**-dependence of $B_{2g}(1)$ mode wavenumber in both films and ceramics to look for the elastic behaviour of the oxygen octahedra. Figure 6b) shows the the **x**-dependence of $B_{2g}(1)$, besides the $\Delta\mathbf{d}_{Mn\text{-}O2}/\mathbf{d}_{Mn\text{-}O2}$ ratio, which was calculated from the relation $\boldsymbol{v} \propto (\mathbf{d}_{Mn\text{-}O2})^{-3/2}$ [22]:

$$\frac{\Delta \mathbf{d}_{Mn-O2}}{\mathbf{d}_{Mn-O2}}(\mathbf{x}) = -\frac{2}{3}\frac{\nu_f(\mathbf{x})-\nu_c(\mathbf{x})}{\nu_c(\mathbf{x})}. \qquad (3)$$

where $\boldsymbol{v}_f$ and $\boldsymbol{v}_c$ stand for the $B_{2g}(1)$ mode wavenumbers in films and ceramics , respectively. the $B_{2g}(1)$ mode wavenumber follows a relative increase of with **x**, this trend is more apparent for films with **x** >0.2. It is worth noting that a slight compression of the octahedra is also observed for ceramics while **x** increases. Nonetheless, this compression is more significant in films, which can reach a maximum value of ~0.5% for **x** = 0.4. Hence, these results, are a solid indication that the compressive elastic energy for higher values of Lutetium concentration is mainly accommodated in the tightening of oxygen octahedra. Though not corresponding to any primary Raman active modes of

the *Pnma* symmetry, The Raman spectra show the emergence of two additional bands observed at ~218 cm^{-1} and at ~690 cm^{-1}. This feature is considered as Raman activation of infrared modes observed in $EuMnO_3$ ceramics [25], possibly associated with localized lowering of symmetry distortions occurring in the film region close to the cubic substrate. As previously referred to, the film lattice compression prompts the increase of the Mn-O1-Mn angle and the decrease of the Mn-O2 bond, these structural distortions have significant impact on electronic orbital overlapping and are the main parameters prompting the transfer integral which affect the superexchange magnetic interactions, hence yielding relevant consequences on the magnetic properties of the thin films [26].

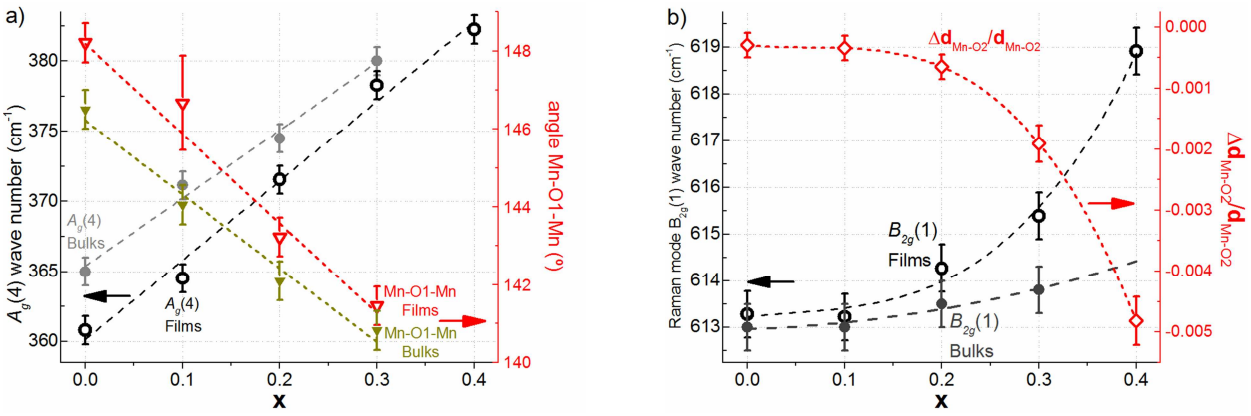

Figure 6: **x**-dependence of a) A_g(4) tilting mode and Mn-O1-Mn bond angle; b) B_{2g}(1) symmetric stretching mode and $\Delta\mathbf{d}_{Mn\text{-}O2}/\mathbf{d}_{Mn\text{-}O2}$, for films (open symbols) and ceramics (solid symbols) [9] at room temperature.

In order to study the impact on magnetic properties of the film lattice distortions and substrate strain, were performed measurements in the as-prepared films of induced magnetization (***M***) and the magnetic hysteresis cycles as function of temperature with particular focus on the temperature range from 5 to 120 K, where relevant magnetic phase transitions occur in the rich phase diagram of the corresponding ceramics [27, 26, 29]. Figure 7a) shows the temperature dependence of ***M***, obtained in zero-field cooling (ZFC) and field cooling (FC) conditions under 100 Oe bias magnetic field, for the discrete values of **x** from 0.0 to 0.4. For **x** = 0.0 the confluence between the ZFC and FC enables to ascertain $\mathbf{T}_N$ ~ 45 K, below which is found the characteristic weak ferromagnetism arising from the canted A-type AFM observed in $EuMnO_3$ [26, 27]. For sequent films with increasing Lu concentration, the overall magnitude of the ***M***(**T**) curves decreases monotonically, particularly below 50 K the difference between FC and ZFC curves also tends to decrease and the concavity under FC conditions tends to inflect downward. These incidences suggest that the canted magnetic structure can be understood assuming a consistent strengthening of the ferromagnetic character. Furthermore, for $\mathbf{x} \geq 0.1$ the ZFC and FC curves do not merge directly into one another which prevents the precise determination of $\mathbf{T}_N$ since a clear transition from a paramagnetic to a canted A-type AFM cannot be so easily perceived. Figures 7b) show representative magnetic hysteresis loops ***M***(***B***) at different fixed temperatures (subtracted from the linear paramagnetic contribution from substrate) for **x** = 0.0; 0.1: 0.2; 0.3 and 0.4. It is patent that the substituted films exhibit some weak ferromagnetic character induced by the external magnetic field, which is not noticeable for the ceramics. As example, for **x** = 0.1 a FM contribution is a perceptible even at 100 K exhibiting a remanence $\boldsymbol{M}_r$ ~ 0.15 $emu.g^{-1}.cm^{-3}$, a coercive field $\boldsymbol{B}_c$ >0.007 Tesla and saturation at ~2 Tesla. Whereas for the film with **x** = 0.0 at 80 K, $\boldsymbol{M}_r$ ~ 0.01 $emu.g^{-1}.cm^{-3}$ and $\boldsymbol{B}_c$ <0.001 which is near the SQUID measurement system detection limits. Even though, the observed differences between ZFC and FC curves above 50 K seem relevant, that does not necessary mean the occurrence of long range FM order throughout the whole film. The films phase based in a canted antiferromagnetic character combined with the presence of a highly-stressed interface between film and substrate can create the adequate conditions to constrain a region with pinned magnetic moments induced by a low bias magnetic field [30]. This localized effect, which is also compatible with the aforementioned interpretation of Raman activation of infrared modes, can emulate a ferromagnetic response and justify the presence of the induced hysteresis detected at higher temperatures.

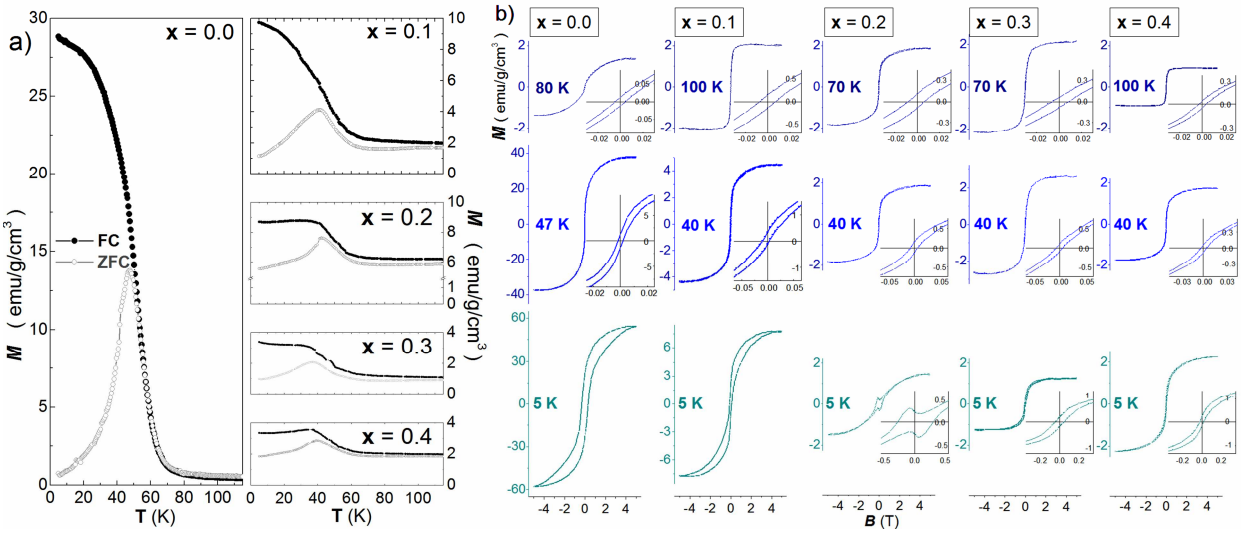

Figure 7: a) Temperature dependence of the induced magnetization with $0 \leq \mathbf{x} \leq 0.4$, measured under ZFC (○) and FC (●) conditions at 100 Oe. b) Representative $\boldsymbol{M}(\boldsymbol{B})$ for **x** = 0.0; 0.1; 0.2; 0.3 and 0.4 thin films at different temperatures and respective insets zooming hysteresis loops in low field region.

CONCLUSIONS

$Eu_{1-x}Lu_xMnO_3$ thin films with $0 \leq \mathbf{x} \leq 0.4$ were deposited successfully in the pseudo-perovskite phase onto $Pt/Ti/SiO_2/Si(100)$ substrates, while in ceramics this phase is limited to $\mathbf{x} \leq 0.2$. Thin films properties concerning structure, lattice dynamics and magnetic response are significantly different from bulk samples with matching composition reported in literature. The alterations and behaviors of the as-prepared films can be understood by assuming a compressive state in the film induced by mechanical coupling with the substrate. For low **x** values the compressive elastic energy is oriented to Mn-O1-Mn tilt angle broadening, while for higher **x** values it is mainly accommodated in contracting the oxygen octahedral Mn-O2 bond. Such structural distortions even enable the Raman activation of typical infrared modes. Substituted films show a smearing out of the paramagnetic-canted A-type AFM transition, also exhibiting a peculiar weak induced ferromagnetic response even up to 100 K, contrarily to ceramics. The overall behavior of the films can be interpreted on the basis of magnetoelastic coupling, which by changes of electronic orbital overlapping induces important alterations in the magnetic super-exchange interactions yielding noteworthy modifications in the magnetic behavior of the films.

ACKNOWLEDGMENTS

This work was supported by national funds through the FCT/MEC and when appropriate co-financed by FEDER under the PT2020 Partnership Agreement through grant SFRH/BPD/80663/2011 and projects. PTDC/FIS/NAN/0533/2012; IFIMUP-IN: NORTE-01-0145-FEDER-022096 and NECL; CICECO-AIM: POCI-01-0145-FEDER-007679, UID/CTM/50011/2013 and PTDC/FIS-NAN/0533/2012; Fundação CAPES: PNPD-UFAM/Física, no: 1671526.

REFERENCES

[1] W. Eerenstein, N. D. Mathur, J.F. Scott, Nat. 2006, **442**, 759-765.

[2] S. Lee, A. Pirogov, M. Kang, K. H. Jang, M. Yonemura, T. Kamiyama, S. W. Cheong, F. Gozzo, N. Shin, H. Kimura, Y. Noda, J. G. Park, Nat. 2008, **451**, 805-808.

[3] M. Fiebig, J. Phys. D. Appl. Phys. 2005, **38**, R123-R152.

[4] S.-W. Cheong, M. Mostovoy, Nat. Mater. 2007, **6**, 13-20.

[5] S. Dong, J. M. Liu, Mod. Phys. Lett. B 2012, **26**, 1230004.

[6] J. Park, J. G. Park, G. S. Jeon, H. Y. Choi, C. H. Lee, W. Jo, R. Bewley, K. A. McEwen, T.G. Perring, Phys. Rev. B 2003, **68**, 104426.

[7] T. Choi, Y. Horibe, H. T. Yi, Y. J. Choi, W. Wu, S. W. Cheong, Nat. Mater. 2010, **9**, 253-258.

[8] F. G. Figueiras, D. Karpinsky, P. B. Tavares, J. N. Gonçalves, S. Y.-Vilar, A. F. M. Dos Santos, A. Franz, M. Tovar, J. A. Moreira, V. S. Amaral, Phys. Chem. Chem. Phys. 2017, **19**, 1335-1342.

[9] D. A. Mota, Y. R.-Barcelay, P. B. Tavares, M. R. Chaves, A. Almeida, J. Oliveira, W. S. Ferreira, J. A. Moreira, J. Phys. Condens. Matter 2013, **25**, 235602.

[10] J. Oliveira, J. A. Moreira, A. Almeida, M. R. Chaves, J. M. M. da Silva, J. B. Oliveira, M. A. Sá, P. B. Tavares, R. Ranjith, W. Prellier, Phys. Rev. B 2011, **84**, 094414.

[11] Y. R.-Barcelay, J. A. Moreira, A. Almeida, J. P. Araújo, J. P. de la Cruz, Materials Letters 2012, **70**, 167-170.

[12] Y. R.-Barcelay, J. A. Moreira, G. G.-Aguilar, A. Almeida, J. P. Araujo, J. P. de la Cruz, J. Electroceram. 2011, **26**, 44-55.

[13] W. Hu, C. Yang, W. Zhang, G. Liu, D. Dong. J. Sol-Gel Sci. Techn. 2006, **39**, 293-298

[14] J. Rodriguez-Carvajal, Physica B 1993, **55**, 192.

[15] J. Agostinho Moreira, A. Almeida, M. R. Chaves, M. L. Santos, P. P. Alferes, I. Gregora, Phys. Rev. B 2007, **76**, 174102.

[16] X. Llovet, C. Merlet, Microsc. Microanal. 2010, **16**, 21-32

[17] T. Mori, N. Kamegashira, K. Aoki, T. Shishido, T. Fukuda; Materials Letters 2002, **54**, 238-243.

[18] R. D. Shannon, Acta Crystallogr A. 1976, **32**, 751-767

[19] A. Vailionis, H. Boschker, W. Siemons, E. P. Houwman, D. H. A. Blank, G. Rijnders, and G. Koster. Physical Rev. B 2011, **83**, 064101.

[20] T. Kimura, S. Ishihara, H. Shintani, T. Arima, K. T. Takahashi, K. Ishizaka, Y. Tokura, Phys. Rev. B 2003, **68**, 060403 (R).

[21] E. Sánchez, T. López, R. Gómez, Bokhimi, A. Morales, O. Novaro, J. Solid State Chem. 1996, **122**, 309-314.

[22] P. M. Woodward, T. Vogt, D. E. Cox, A. Arulraj, C. N. R. Rao, P. Karen, A. S. K. Cheetham, Chem. Mater. 1998, **10**, 3652-3665.

[23] M. N. Iliev, M. V. Abrashev, J. Laverdière, S. Jandl, M. M. Gospodinov, Y.-Q. Wang, Y.-Y. Sun, Phys. Rev. B 2006, **73**, 064302, 1-6.

[24] M. C. Weber, M. Guennou, H. J. Zhao, J. Íñiguez, R. Vilarinho, A. Almeida, J. A. Moreira, J. Kreisel, Phys. Rev. B 2016, **94**, 214103, 1-8.

[25] W. S. Ferreira, et al, Phys. Rev. B 2009, **79**, 054303.

[26] V. Y. Ivanov, A. A. Mukhin, V. D. Travkin, A. S. Prokhorov, Yu. F. Popov, A. M. Kadomtseva, G. P. Vorobev, K. I. Kamilov, A. M. Balbashov , Phys. Status Solidi B 2006, **243**, 107-111.

[27] J. Hemberger, F. Schrettle, A. Pimenov, P. Lunkenheimer, V. Yu. Ivanov, A. A. Mukhin, A. M. Balbashov, A. Loidl, Phys. Rev. B 2007, **75**, 035118.

[28] J. Agostinho Moreira, et al., Solid State Comm. 2011, **151**, 368-371.

[29] J. A. Moreira, A. Almeida, W. S. Ferreira, J. E. Araújo, A. M. Pereira, M. R. Chaves, Phys. Rev. B 2010, **81**, 054447, 1-12.

[30] F.G. Figueiras, D. Dutta, N.M. Ferreira, F.M. Costa, M.P.F. Graça, M.A. Valente, Materials & Design 2016, **90**, 829-833.

HIGHLIGHTS:

- $Eu_{1-x}Lu_xMnO_3$ Orthorhombic phase in thin films extends to $0 \leq x \leq 0.4$ while the bulk ranges $0 \leq x \leq 0.2$.
- Raman spectroscopy allows to estimate the relative variation of Mn-O1-Mn bond angle with x.
- Thin film structural distortions encompass both compression and alignment of MnO_6 octahedra.
- Thin film phase exhibits an additional ferromagnetic contribution not found in bulk form.